separations

MDPI

Article

The Formation Mechanism of the Crystal Morphology of Guanidinoacetic Acid: Selective Adsorption of Additives and Solute Diffusion

Xin Chen [1], Yifan Li [1], Qian Wu [1], Ting Wang [1,2,*], Na Wang [1,2], Lina Zhou [1,2,*], Hongxun Hao [1,2] and Jingkang Wang [1,2]

[1] National Engineering Research Center of Industrial Crystallization Technology, School of Chemical Engineering and Technology, Tianjin University, Tianjin 300072, China; 2023207055@tju.edu.cn (X.C.); 2024439203@tju.edu.cn (Y.L.); wuqianok@tju.edu.cn (Q.W.); wangna224@tju.edu.cn (N.W.); hongxunhao@tju.edu.cn (H.H.); jkwang@tju.edu.cn (J.W.)

[2] Collaborative Innovation Center of Chemical Science and Engineering (Tianjin), Tianjin 300072, China

* Correspondence: wang_ting@tju.edu.cn (T.W.); linazhou@tju.edu.cn (L.Z.)

Abstract

Guanidinoacetic acid (GAA), an important feed additive, shows poor powder properties due to its morphological characteristics. In this study, GAA was employed as a model compound to investigate the regulatory effects of polymeric additives (hydroxypropyl methyl cellulose, hydroxypropyl cellulose, and polyacrylamide) on its crystal growth and powder properties through integrated experimental and molecular simulation approaches. In situ single-crystal growth experiments reveal that hydroxypropyl methyl cellulose (HPMC) and hydroxypropyl cellulose (HPC) can selectively suppress the growth of the (11–1) crystal face while slightly promoting the growth of the (011) crystal face, thereby altering the relative growth rates and modifying the final crystal morphology. However, polyacrylamide (PAM) inhibits the growth of both the (11–1) and (011) crystal faces, resulting in negligible alteration of GAA crystal morphology. Growth kinetic analysis indicates that crystal growth is governed by a surface integration-controlled mechanism. Molecular dynamics simulations further demonstrate that the additive preferentially adsorbs onto specific crystal faces, reducing interfacial solute accumulation and inhibiting molecular diffusion. Collectively, these findings demonstrate that additives exert synergistic control over crystal morphology and particle size distribution through selective adsorption and modulation of interfacial mass transfer. This research provides mechanistic insights and theoretical guidance for the regulation of crystallization processes via additive intervention.

Keywords: guanidinoacetic acid; crystal growth; morphology modification; additives; powder property

Check for updates

Academic Editor: Gavino Sanna

Received: 16 April 2026
Revised: 19 May 2026
Accepted: 22 May 2026
Published: 24 May 2026

Copyright: © 2026 by the authors. Licensee MDPI, Basel, Switzerland. This article is an open access article distributed under the terms and conditions of the Creative Commons Attribution (CC BY) license.

1. Introduction

Crystal morphology (or crystal habit) plays a critical role in determining the downstream processability and product properties of crystal products. In terms of downstream processing, variations in crystal morphology significantly influence filtration and separation performance, drying efficiency, powder flowability, and caking tendency [1–4]. In terms of crystal product performance, for instance, one-dimensional perovskite structures facilitate carrier transport and are advantageous for photodetection. Two-dimensional structures—owing to strong quantum confinement and a large specific surface area—are

more suitable for light absorption and charge separation [5]. Besides, diverse nanocrystal morphologies enable localized surface plasmon resonance, which holds significant importance in catalysis, spectroscopy, and sensing applications [6,7]. Consequently, crystal habit engineering has emerged as a key strategy for enhancing product quality and ensuring the stability of crystallization processes.

Among various crystal habit modification strategies, the additive-mediated approach is widely employed due to its efficiency and operational flexibility [8,9]. By selectively adsorbing onto specific crystal faces, additives can modulate the relative growth rates of different crystal faces, thereby controlling the overall crystal morphology [10,11]. Existing research has predominantly focused on small-molecule additives (e.g., amino acids and surfactants), which mainly influence crystal growth through hydrogen bonding, electrostatic interactions, and steric hindrance effects [12–14]. However, in certain systems, small-molecule additives exhibit limitations in terms of product purity and the achievable range of morphological control [15]. In contrast, polymeric additives have attracted considerable attention in recent years owing to their flexible chain architectures, wide coverage capability and multifunctional characteristics [16,17]. Such attributes enable multivalent interactions with crystal surfaces, facilitating the formation of relatively stable adsorption conformations. For example, Nicolau and Matzger [18] selected three commercial polymers—polyvinylpyrrolidone, polyvinyl alcohol, and polyethylene glycol—as face-selective shape modifiers for the explosive compounds. By targeting intermolecular interactions found in cocrystals, they achieved both desirable (needle-to-block) and undesirable (block-to-needle) morphology changes. Bellucci et al. [19] examined four polymer additives at low concentrations for their effect on metformin HCl crystal habit. Using both crystallization experiments and computational modeling, they showed that the additives selectively adsorb onto the slow-growing (100) and (020) crystal faces, altering the relative growth rates and thereby modifying the crystal morphology. Hatcher et al. [20] used soluble, non-size-matched polymer additives at very low concentrations (0.5 wt %) to control the crystal habit of the active pharmaceutical ingredient lovastatin. The hydrophilic polymer poly(ethylene glycol) promoted the formation of longer, thinner needles, whereas the hydrophobic polymer poly(propylene glycol) improved the habit from needles toward plate-like crystals. Nonetheless, the efficacy of additives typically results from a superposition of multiple mechanisms due to the complexity of crystallization environments [21,22]. The precise molecular-level mechanism underlying the regulatory behavior of polymeric additives requires further elucidation.

Guanidinoacetic acid (GAA) is an important feed additive [23,24], biosynthetic intermediate [25], and material-modifying agent [26,27]. Under conventional crystallization conditions, GAA typically forms plate-like crystal morphologies or a powdery solid. Crystals of such morphology often exhibit poor flowability and are prone to agglomeration and caking, thereby adversely affecting industrial production and downstream processing. Although preliminary studies have been conducted on the crystallization behavior of GAA [28], systematic research on crystal habit modification—particularly through the use of polymeric additives—remains relatively limited. More importantly, despite recent efforts to elucidate the crystallization process from a molecular perspective, there remains a notable need for multiscale mechanistic studies that systematically correlate macroscopic crystal morphology with molecular-level interactions.

In this study, we systematically investigate the modulating effects of three representative polymeric additives—hydroxypropyl methylcellulose (HPMC), hydroxypropyl cellulose (HPC) and polyacrylamide (PAM)—on the crystal morphology of GAA. By integrating experimental characterization with molecular simulations, the mechanistic role of these additives in modulating crystal growth is elucidated. Firstly, face-specific growth rates

were quantified and subjected to growth kinetic modeling. Subsequently, a mechanistic understanding of polymeric additive-mediated crystal habit modification was developed based on molecular simulations. Finally, the particle properties of GAA products were comprehensively evaluated to assess the effects of the selected additives. This work advances the rational design of polymeric additives and provides actionable guidance for optimizing industrial crystallization processes of GAA.

2. Materials and Methods

2.1. Materials and Reagents

GAA was provided by Tianjin Heowns Biochemical Technology Co., Ltd. (Tianjin, China). PAM and HPMC were purchased from Tianjin Heowns Biochemical Technology Co., Ltd. (Tianjin, China), and HPC was purchased from Shanghai Meril Biochemical Technology Co., Ltd. (Shanghai, China). The above chemicals were directly used without further purification, and their structural formulas are presented in Figure 1. More detailed information related to the chemical materials is listed in Table S1.

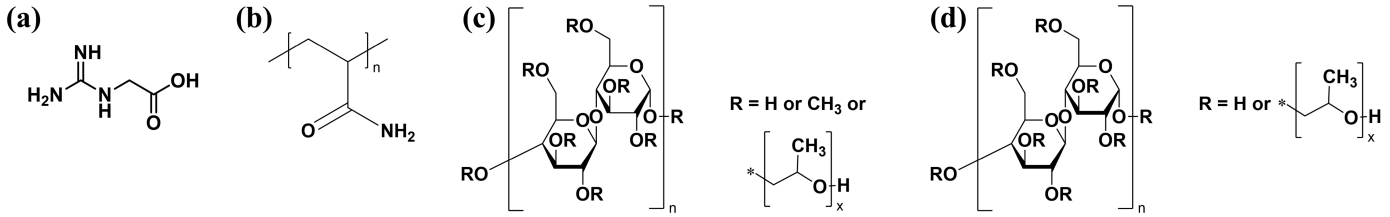


Figure 1. Molecular structure: (**a**) GAA, (**b**) PAM, (**c**) HPMC, (**d**) HPC.

2.2. Solubility Measurement

The solubility (x) of GAA in different solutions (with an additive concentration of 100 ppm) was determined by the UV-vis method at 283.15–323.15 K [29,30]. The ultraviolet detection wavelength was set at 208 nm [31]. The aqueous additive solution with the same dilution factor as the sample to be tested was used as the reference solution to eliminate the influence of the additive's ultraviolet absorption.

Supersaturation (S) is defined as follows:

$$S = \frac{x}{x_0} \tag{1}$$

where x is the solubility of GAA (mol/mol), and x_0 is the solubility (mol/mol) of GAA at the specific temperature (298.15 K in this study).

The modified Apelblat model and NRTL model were employed to fit the solubility data. The modified Apelblat equation is given in Equation (2). NRTL equation and relative parameters are shown in Equations (3)–(6), respectively.

$$lnx = A + \frac{B}{T} + ClnT \tag{2}$$

$$ln\gamma_i = x_j^2\left[\frac{\tau_{jiG_{ji}^2}}{\left(x_i + x_jG_{ji}\right)^2} + \frac{\tau_{ijG_{ij}^2}}{\left(x_j + x_iG_{ij}\right)^2}\right] \tag{3}$$

$$ln\gamma_j = x_i^2\left[\frac{\tau_{ijG_{ij}^2}}{\left(x_j + x_iG_{ij}\right)^2} + \frac{\tau_{jiG_{ji}^2}}{\left(x_i + x_jG_{ji}\right)^2}\right] \tag{4}$$

$$G_{ji} = exp\left(-\alpha_{ij}\tau_{ji}\right)\ \ G_{ij} = exp\left(-\alpha_{ij}\tau_{ij}\right) \tag{5}$$

$$\tau_{ji} = \frac{g_{ji} - g_{ii}}{RT} \quad \tau_{ij} = \frac{g_{ij} - g_{jj}}{RT} \tag{6}$$

where T is the temperature (K), and A, B, C are parameters of the modified Apelblat model. γ_i represents the activity coefficient of component i; G and g denote the local composition factor and interaction energy parameter, respectively; α_{ij} is the non-randomness parameter, which quantifies the deviation of the local composition from a random mixture. For weakly polar or non-polar systems, α_{ij} typically ranges from 0.2 to 0.3, while for strongly polar systems or those involving hydrogen bonding, it ranges from 0.3 to 0.47 [32].

The average relative deviation (*ARD*) and the root-mean-square deviation (*RMSD*) were employed as metrics to evaluate model fitting performance. Their equations are given below.

$$ARD = \frac{1}{N}\sum_{i=1}^{N}\left|\frac{x_i^{exp} - x_i^{cal}}{x_i^{exp}}\right| \tag{7}$$

$$RMSD = \left[\frac{1}{N}\sum_{i=1}^{N}\left(x_i^{exp} - x_i^{cal}\right)^2\right]^{1/2} \tag{8}$$

where N is the number of data points, x^{exp} is the solubility obtained experimentally, and x^{cal} is the solubility obtained from the model fitting.

2.3. Crystallization Experiments

2.3.1. Crystal Morphology Experiments

A series of controlled cooling crystallization experiments were conducted to systematically investigate the effect of additives on the crystal morphology of GAA. Specifically, 200 g of a pre-prepared solution—either pure water or an aqueous solution containing the additive—was introduced into the crystallizer. Based on experimentally determined solubility data, an appropriate quantity of GAA was added to prepare a saturated solution at 353.15 K. The mixture was stirred and heated to 363.15 K, then held at this temperature for 30 min to ensure complete dissolution. Subsequently, the solution was cooled linearly to 343.15 K at a controlled rate of 20 K·h^{-1} and maintained isothermally for 1 h. During the isothermal hold stage, 0.5 wt% seed crystals (relative to solute mass, 100–140 mesh) were introduced. The system was then further cooled to 293.15 K at 6 K·h^{-1} and aged for an additional 1 h. Finally, the resulting crystals were recovered by vacuum filtration, washed with deionized water, dried under ambient conditions, and subjected to morphological and structural characterization.

2.3.2. Secondary Nucleation Determination

To investigate the influence of additives on the secondary nucleation behavior of GAA, the induction time for secondary nucleation was estimated. The experimental protocol followed that detailed in Section 2.3.1, with all operations conducted under rigorously controlled thermal and hydrodynamic conditions. Real-time monitoring of particle number was performed using a Particle Counting and Monitoring (PCM) crystallization system. Specifically, the time of seeding (t_0) and the time at which the detected particle counts began to rise sharply (t_n) were recorded. In this work, the secondary nucleation induction time (t_{ind}) was defined as the temporal interval between these two precisely identified events.

$$t_{ind} = t_n - t_0 \tag{9}$$

2.3.3. Characterization

Solid-State Characterization

The morphology of GAA crystals was characterized using scanning electron microscopy (SEM, TM 3000, Hitachi, Tokyo, Japan). Prior to analysis, the samples were sputter-coated with a gold layer (~200–400 Å) using a magnetron sputtering device (MPS-1S). Powder X-ray diffraction (PXRD, MiniFlex600, Rigaku, Tokyo, Japan) was employed to analyze the crystalline phases of samples obtained under different additive conditions. The measurements were conducted at 40 kV and 200 mA over a 2θ range of 5–60° and a scanning rate of 10°/min. Fourier transform infrared spectroscopy (FTIR, ALPHA, Bruker, MA, USA) was used to assess potential additive residues in the crystals over a spectral range of 4000–400 cm^{-1}. Further characterization of impurity content in GAA crystals was performed using proton nuclear magnetic resonance spectroscopy (^{1}H NMR, AVANCE, Bruker, MA, USA). The analyses were carried out at 298.15 K with a 400 MHz liquid-state NMR spectrometer, accumulating 32 scans for each spectrum. All chemical shifts (δ) were referenced to tetramethylsilane (TMS) as the internal standard.

Face Indexing

Crystal face indices were determined by X-ray single-crystal diffractometer (XtaLAB FrX, Rigaku, Tokyo, Japan). Prior to data acquisition, the crystal was mounted on a goniometer head and carefully aligned. Systematic φ-scans were then carried out with a step size of 1° per frame to collect diffraction intensities from multiple crystallographic orientations. The crystallographic faces were subsequently indexed based on the integrated reflection data, following empirical absorption correction and full structural refinement using CrysAlisPro software (version 1.171.44.91a).

Particle Size Distribution

Laser diffraction analysis of GAA products obtained with different additives was conducted using a Mastersizer 3000 instrument. The coefficient of variation (*C.V.*) was calculated according to Equation (10) to evaluate the particle size distribution (PSD).

$$C.V. = \frac{100(R_{84\%} - R_{16\%})}{2R_{50\%}} \quad (10)$$

where $R_{16\%}$, $R_{50\%}$, and $R_{84\%}$ represent the particle diameters corresponding to cumulative volume fractions of 16%, 50%, and 84%, respectively.

Flowing Performance

Powder flowability was evaluated quantitatively using three established parameters: the Carr Compressibility Index (*CI*), the Hausner Ratio (*HR*), and the angle of repose [33,34]. The angle of repose is defined as the maximum angle between the free surface of a conical powder pile and the horizontal plane under static equilibrium conditions. Both *CI* and *HR* are dimensionless indices derived from bulk density and tapped density, calculated according to the following standardized equations:

$$CI = \frac{TD - BD}{TD} \times 100\% \quad (11)$$

$$HR = \frac{TD}{BD} \quad (12)$$

where *TD* denotes the tap density, while *BD* represents the bulk density.

Anti-Caking Performance

The caking propensity of GAA products was evaluated using a sieve-based method [35,36]. Specifically, the sample was first classified using a sieve with a defined aperture. Subsequently, 2.0 g of GAA was accurately weighed and uniformly spread onto a weighing dish. Approximately 0.5 g of water was then sprayed onto the sample using a spray bottle. The dish was placed in a temperature- and humidity-controlled chamber maintained at 40 °C and 75% relative humidity. The sample was periodically weighed until the total mass reached a constant value. After equilibration, the sample was removed and gently sieved again using the same mesh size to separate agglomerated particles, with care taken to avoid breakage of the agglomerates. The caking ratio is defined as the mass fraction of agglomerated particles relative to the total sample mass, representing the extent of caking.

$$c = \frac{m}{M} \times 100\% \tag{13}$$

where c is the caking ratio, m is the mass of the agglomerated GAA, and M is the total mass of the sample.

2.3.4. Single-Crystal Growth Experiments

The single-crystal growth rates of GAA under varying solution conditions were determined via in situ optical microscopy. Supersaturated solutions with (S = 1.35, 1.40, 1.45, 1.50, 1.55, 1.60, and 1.65) were prepared by dissolving accurately weighed amounts of GAA in pre-equilibrated aqueous media at 318.15 K. The media consisted of either pure water or solutions containing 100 ppm of additive. The resulting solutions were then cooled in a controlled manner to 298.15 K. The resulting 30 mL solutions were filtered through a 0.22 μm filter membrane, then transferred into a temperature-controlled glass crystallization dish containing an orientation-verified GAA seed crystal (200–500 μm). Growth was conducted isothermally at 298.15 K. In situ crystal growth was monitored at fixed time intervals using an inverted optical microscope (Olympus CKX53, Tokyo, Japan, equipped with a high-resolution CCD camera and motorized stage). Face-specific growth rates were calculated from the linear slope of dimensional evolution versus time, with each reported value representing the mean of at least three independent measurements. All experiments were performed in quintuplicate to ensure statistical robustness and reproducibility of the derived growth kinetics.

2.4. Growth Kinetics Models

The crystal growth in the solution is jointly controlled by the transport steps on the solution side and the surface steps at the interface [37]. Based on these processes, some corresponding growth kinetic models have been established in existing studies [38].

$$R = k_g \sigma^g \tag{14}$$

Equation (14) is the most commonly used power-law equation, where k_g represents the growth rate coefficient, g refers to the growth order. When g is above 1, the crystal growth is controlled by the solute incorporation into the growth sites on the crystal surface. Conversely, it indicates that crystal growth is governed by diffusion. σ represents the relative supersaturation.

$$\sigma = S - 1 \tag{15}$$

The crystal growth exhibits a complex dependence on multiple factors, including supersaturation, temperature, particle size, and turbulence intensity [39–41]. Depending on the relationship between the relative supersaturation and growth rate, the crystal

growth process can be categorized into distinct mechanisms: the spiral dislocation growth mechanism (BCF) [37], the two-dimensional nucleation and growth mechanism (B&S) [42], and the continuous growth mechanism (RIG) [43,44]. Under the three distinct crystal growth mechanisms, the growth rate (R) exhibits a quantitative dependence on relative supersaturation (σ), conforming to the relationships given in Equations (16)–(18).

$$R_{BCF} = A_{BCF}\sigma^2 tanh\frac{B_{BCF}}{\sigma} \tag{16}$$

$$R_{B\&S} = A_{B\&S}\sigma^{5/6} exp\frac{B_{B\&S}}{\sigma} \tag{17}$$

$$R_{RIG} = A_{RIG}\sigma \tag{18}$$

where A and B are system-specific constants.

2.5. Molecular Dynamics Simulation

Molecular dynamics (MD) simulations were performed to investigate the influence of additives on the crystallization process at the molecular level. All simulations were carried out using Materials Studio (Accelrys Software Inc., USA, version 2019) with the PCFF force field to describe intermolecular interactions. Prior to the simulations, energy minimization was conducted to obtain stable initial configurations, followed by dynamic simulations under appropriate statistical ensembles to analyze the interactions between additives and crystal surfaces, as well as their effects on solute transport. Detailed computational methods for the molecular dynamics simulation are provided in Supplementary Materials, Part S1.

3. Results and Discussion

3.1. Solubility of GAA

Figure 2a presents the solubility of GAA in the temperature range of 283.15–323.15 K in the presence of different additives (100 ppm). Compared with the results obtained in pure water using the gravimetric method [28], a minor deviation of less than 5% confirmed the accuracy of the final solubility data in this work. It is observed that the addition of additives leads to a slight increase in the solubility of GAA; however, the extent of this enhancement is marginal. This indicates that the additives do not significantly alter the solution supersaturation and, therefore, are unlikely to influence the crystal morphology of GAA through this pathway. Based on the established solubility data, GAA solutions with well-defined supersaturation levels can be accurately prepared throughout the experiments, providing a solid foundation for subsequent investigations of crystallization behavior.

In this study, the modified Apelblat equation and the NRTL equation were employed to correlate the experimental solubility data. The solubility curves generated by these two models are presented in Figure 2b and Figure S4, respectively. The experimental solubility data, along with the corresponding model-predicted values, are summarized in Table S2. The fitted model parameters—as well as the *ARD* and *RMSD*—are detailed in Tables S3 and S4.

The fitting results demonstrate that both models provide satisfactory correlations of the solubility behavior of GAA in the investigated systems. Specifically, for the NRTL model, all *ARD* values are below 3.5%, and all *RMSD* values are less than 0.004%. As for the modified Apelblat equation, it exhibits superior fitting performance, with all *ARD* values below 2% and *RMSD* values less than 0.002%. The lower deviation metrics indicate that the modified Apelblat equation offers improved accuracy and is more suitable for representing the solubility of GAA in solution.

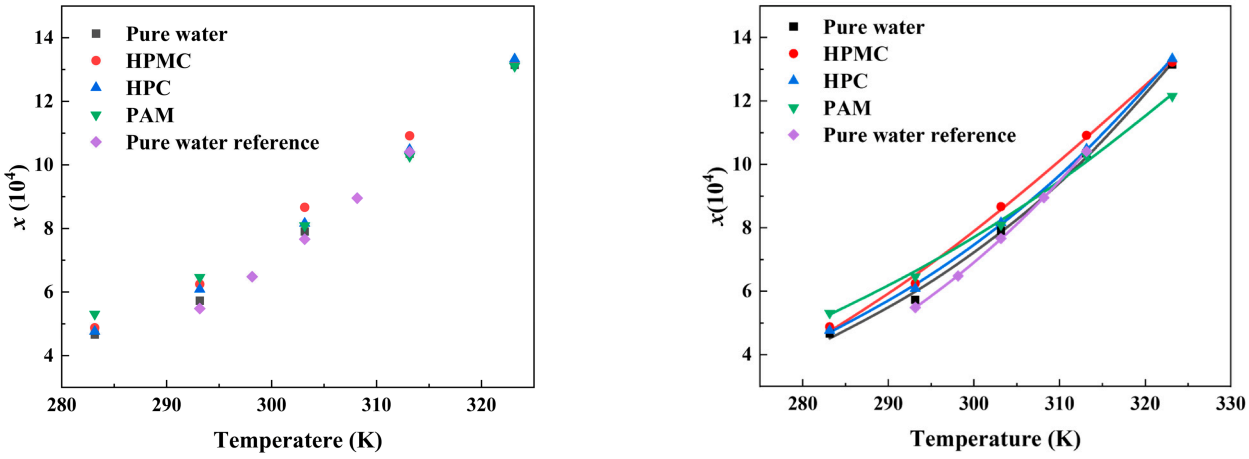


Figure 2. (**a**) Solubility of GAA in solutions containing different additives. (**b**) Solubility curves using the modified Apelblat equation (the points represent the experimental data, and the lines represent the fitted curves).

3.2. Crystal Morphology Characteristics Analysis

Prior to the main crystallization experiments, we systematically evaluated the effect of additive concentration on GAA crystal morphology over the range of 0, 50, 100, 200, and 400 ppm (Figure 3). The results show that morphological differences were minor beyond 50 ppm, indicating that the additive effect approaches saturation at modest concentrations. Therefore, 100 ppm was chosen as a representative working concentration.

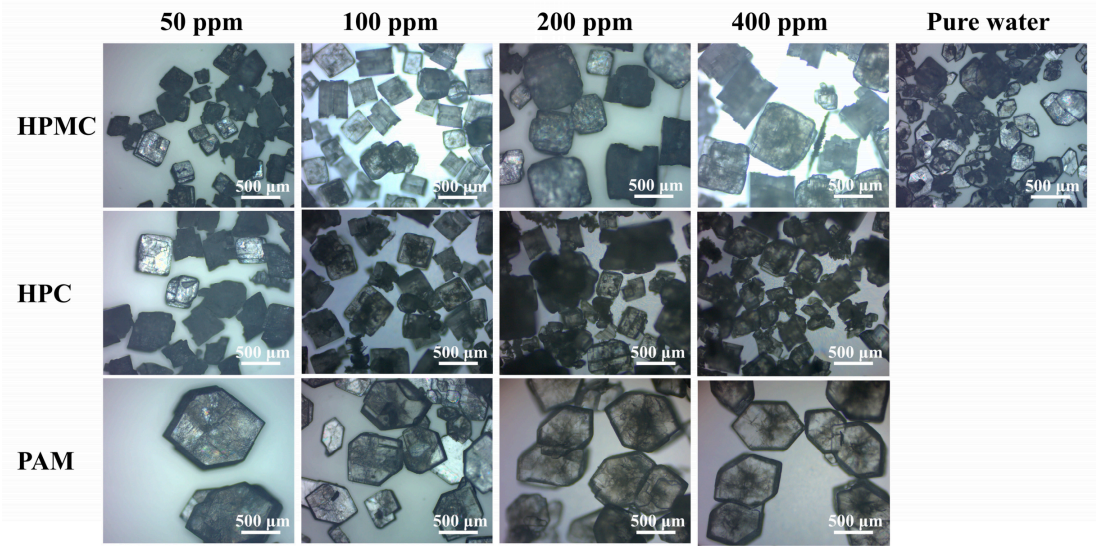


Figure 3. Morphologies of GAA products under different additive concentrations.

Upon cooling crystallization from pure water, hexagonal plate-like single crystals of GAA were obtained; the corresponding Miller indices are depicted in Figure 4. Figure 5 presents the crystal morphologies of GAA under varying polymeric additive conditions. Within the investigated additive concentration range (100 ppm), both HPMC and HPC significantly altered the morphology of the GAA (001) crystal face. The crystal habit of GAA changed from hexagonal platelets to quadrangular, block-like structures, indicating a pronounced habit-modifying effect. In contrast, PAM exerted negligible influence on the geometry of the (001) crystal face. The crystal morphology remained largely unchanged relative to that obtained in the pure aqueous system.

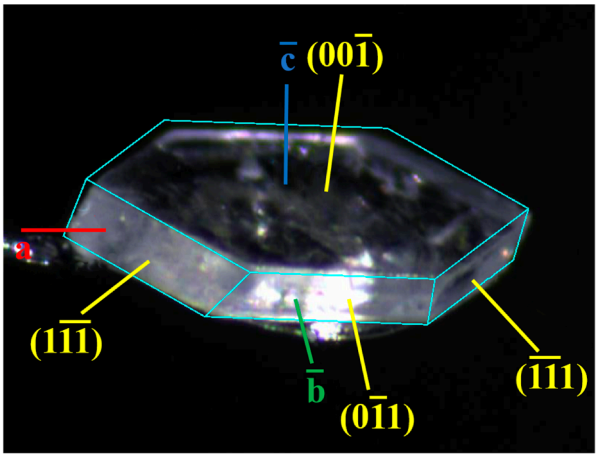


Figure 4. The single crystal obtained in pure water.

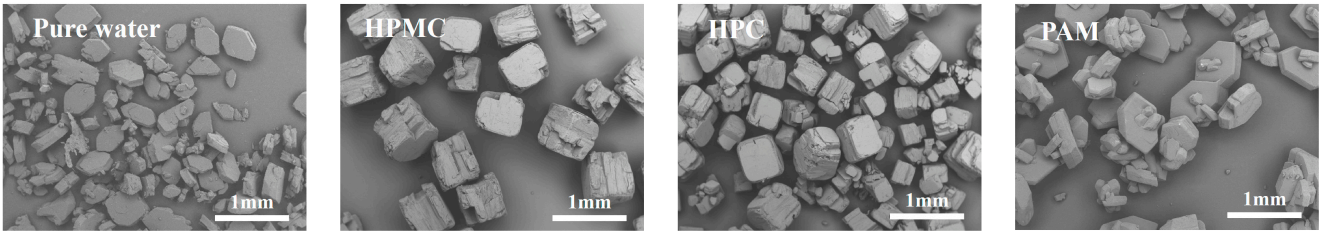


Figure 5. SEM images of GAA crystals obtained from pure water and from solutions containing the polymeric additives.

Moreover, in the presence of all three polymeric additives, GAA crystals display a pronounced increase in thickness along the c-axis. This behavior corresponds to enhanced growth normal to the (001) crystal face.

PXRD and FTIR spectroscopy were employed to characterize the GAA crystals obtained under various additive conditions. As shown in Figure 6, the peak positions in the PXRD patterns of all samples are almost identical, with no emergence of new diffraction peaks or significant peak shifts observed. Only minor variations in peak intensity are detected, indicating that the crystal structure and lattice parameters remain unchanged. Meanwhile, no significant differences were observed in either the positions or intensities of characteristic absorption peaks in the FTIR spectra among various samples. It indicates that the chemical environments of the internal functional groups remained substantially consistent and that the additives were not noticeably retained in the final products. The ^{1}H NMR spectrum shown in Figure 7 further confirms the absence of significant residual additives in the GAA products.

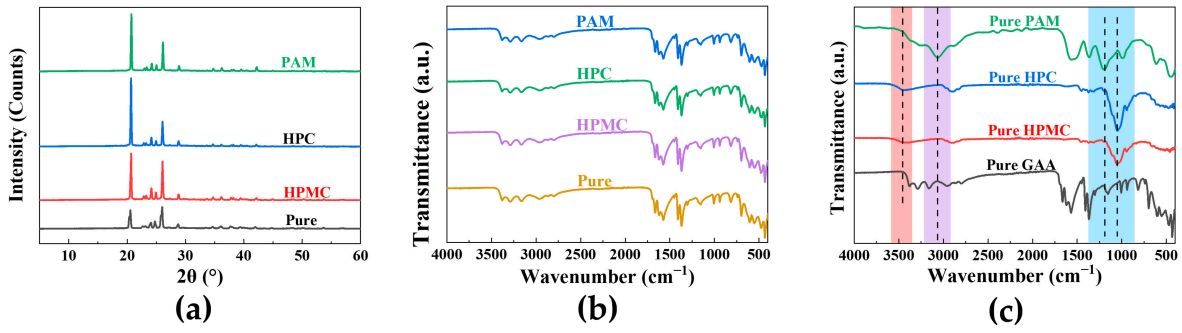


Figure 6. Characterizations of the different products: (**a**) PXRD patterns, (**b**) FTIR spectra of the GAA crystals, (**c**) FTIR spectra of the polymeric additives.

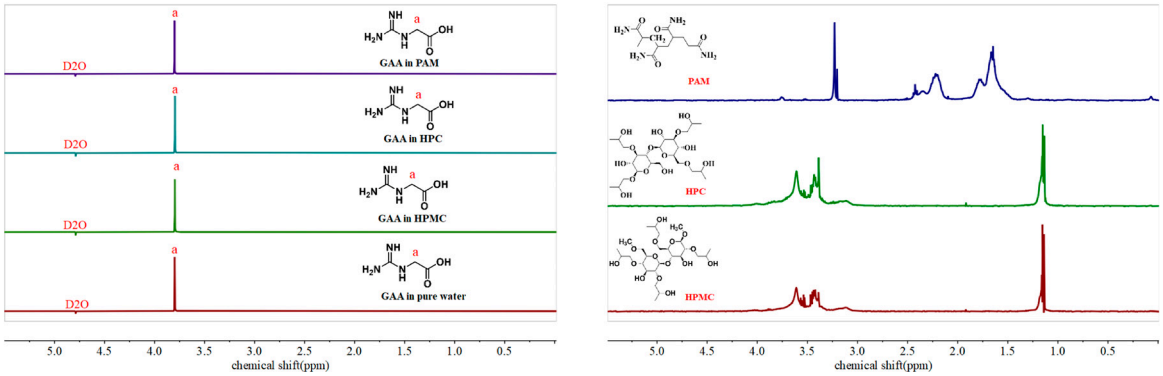


Figure 7. Comparative ^{1}H NMR spectra of the polymeric additives and GAA: (**a**) GAA products obtained under various additive conditions (the characteristic peak at δ = 4.79 ppm corresponds to deuterium oxide), (**b**) pure polymeric additives.

These results demonstrate that, within the investigated concentration range, HPMC, HPC, and PAM did not incorporate into the crystal lattice of GAA. They also did not induce alterations in the molecular structure or the internal packing arrangement of the crystals. Based on the aforementioned observations of crystal morphology evolution, it can be inferred that these polymeric additives primarily modulate the morphology in two ways. They selectively adsorb onto specific crystal faces and/or alter the local solution microenvironment, thereby regulating the relative growth rates of different crystal faces.

3.3. Crystal Growth Analysis

Based on the face indexing analysis, this work conducted a comparative assessment of the absolute and relative growth rates of the (11–1) and (011) crystal faces under various conditions to evaluate the influence of additives on the morphology of GAA. In aqueous solution without additives, GAA adopts a hexagonal plate-like morphology, making it challenging to accurately measure the growth rate along the (001) crystal face. Since variation in the growth rate of the (001) crystal face primarily affects the crystal thickness along its normal direction (i.e., the c-axis direction), the (001) crystal face was not considered in the analysis of additive-induced morphological modifications. The concentration of additives was maintained at 100 ppm in all experiments to ensure consistent comparative conditions. Due to the large total volume of the solution system and the limited number and size of crystals participating in growth, solute consumption during crystallization was negligible relative to the overall system quantity. As shown in Figure S5, the change in the interplanar spacing of GAA crystals exhibits a high degree of linear correlation with time, indicating that the crystals grow stably under a constant supersaturation.

The fitted results of the crystal growth rates of GAA in the presence of polymeric additives are presented in Figures 8, 9, S6 and S7. The corresponding kinetic parameters of the crystal growth models are summarized in Tables S5–S8.

As illustrated in Figure 8, the three selected polymeric additives exhibit two distinct growth-regulating effects on GAA crystals. The addition of PAM marginally inhibits the absolute growth rates of both the (11–1) and (011) crystal faces, with a nearly equivalent degree of inhibition observed for each face. Further analysis in Figure 10 reveals that the relative growth rates of these two crystal faces under PAM exposure remain little changed compared with the pure water system, indicating a limited overall impact on the crystal morphology.

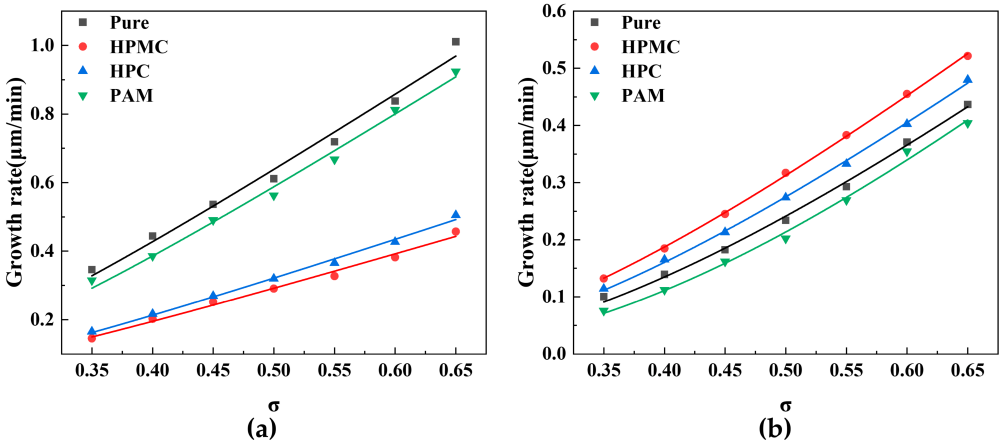


Figure 8. Fitted curves of the B&S model for GAA crystal growth data: (**a**) the (11–1) crystal face, (**b**) the (011) crystal face.

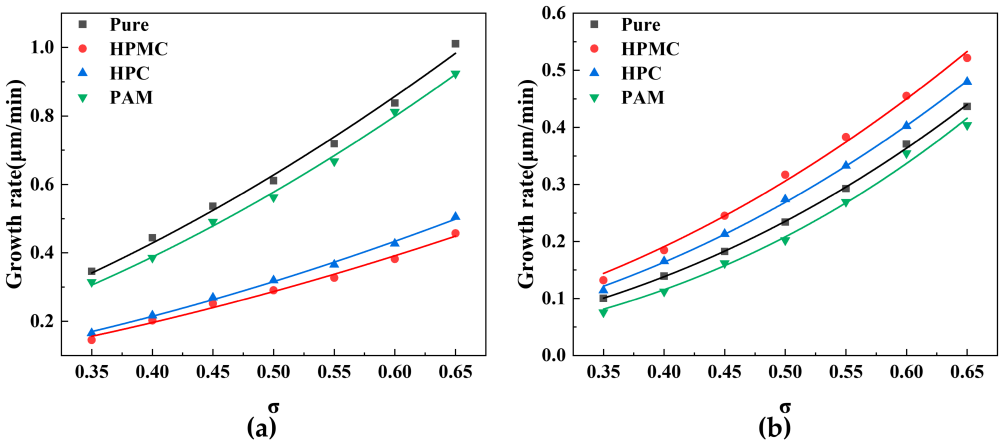


Figure 9. Fitted curves of the empirical equation for GAA crystal growth data: (**a**) (11–1) crystal face, (**b**) (011) crystal face.

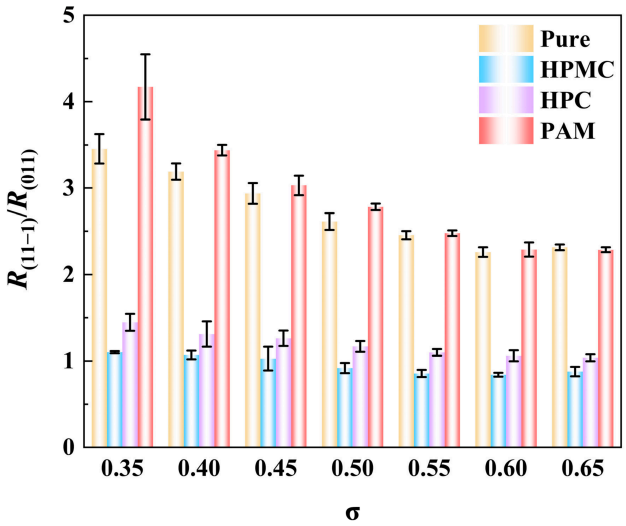


Figure 10. Relative growth rates of the (11–1) and (011) crystal faces of GAA under different conditions.

In contrast, HPMC and HPC exhibit pronounced face-selective regulation of crystal growth rates. HPMC and HPC significantly inhibit the growth of the (11–1) crystal face while slightly promoting that of the (011) crystal face, with HPMC showing a more pronounced effect. Crystal morphology is primarily governed by the slowest-growing

faces [45,46]; suppression of the (11–1) crystal face and its symmetry-equivalent faces leads to their increased exposure, while the relatively faster growth of the (011) crystal face leads to its decreasing exposure. These two together induce morphological reconstruction of the original plate-like structure. Consequently, the crystal morphology evolves from a hexagonal plate-like form to a block-like form.

As indicated in Tables S5–S7 and Figures S8–S10, under various additive conditions, the B&S model consistently exhibits high R^2 values and a relatively random distribution. This demonstrates that, in comparison with the BCF model and the RIG model, the B&S model provides a more accurate characterization of the crystal growth process of GAA. Specifically, GAA molecules first form stable two-dimensional nuclei on the surface; then, driven by supersaturation, molecules preferentially attach to step edges and propagate laterally, leading to step advancement and layer-by-layer crystal growth [47–49]. As shown in Figures 9 and S11, the empirical equation also demonstrates a superior fit. The growth orders (g) are greater than 1.70, suggesting that the crystal growth process of GAA is not controlled by volume diffusion but by solute surface integration.

3.4. Mechanism of Additive-Induced Morphological Regulation of GAA

3.4.1. Additives' Behavior near the Crystal Surface

Experimental results indicate that distinct polymeric additives exhibit significant selective regulation effects on the growth rates of various crystal faces, leading to marked alterations in crystal morphology. The crystal growth process fundamentally involves the adsorption and integration of solute molecules at crystal faces. Based on this understanding, an additive–crystal interface model was initially established in this study to analyze the adsorption behavior of additives on different crystal faces.

Figure 11 shows the evolution of interaction energy between polymer chains and different crystal faces of GAA. On the (11–1) crystal face, HPMC and HPC exhibit pronounced fluctuations at the initial stage due to the non-equilibrium adsorption process. The system subsequently approaches equilibrium, with the interaction energy stabilizing at approximately −150 kcal/mol. In contrast, on the (011) crystal face, the interaction energies of all three additives remain relatively stable throughout the simulation.

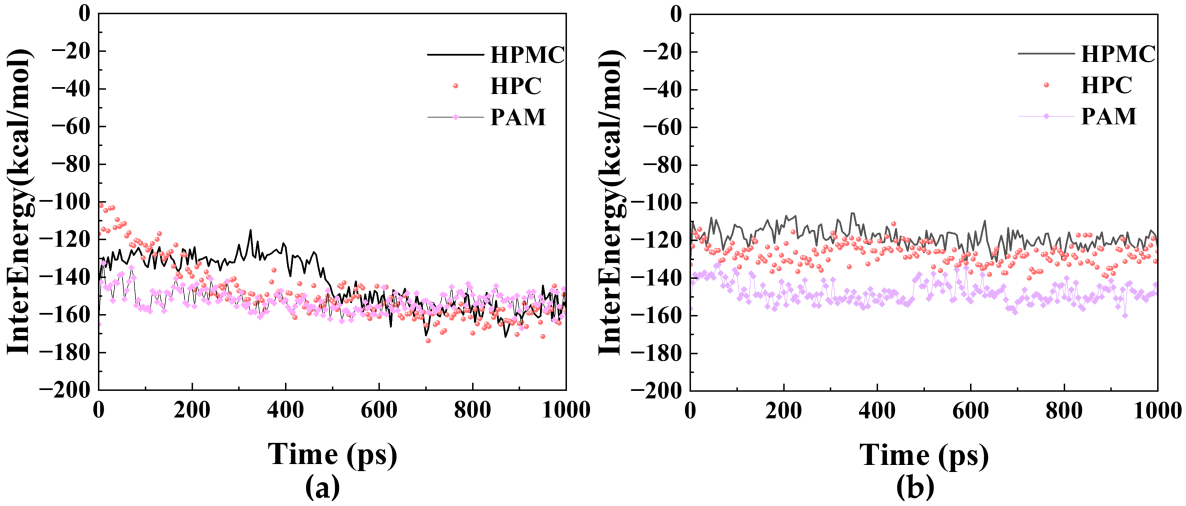


Figure 11. Variation in interaction energy between additives and crystal faces over simulation time: (**a**) (11–1) crystal face, (**b**) (011) crystal face.

The averaged interaction energies during the adsorption equilibrium stage are summarized in Figure 12. All interaction energies are negative, indicating thermodynamically spontaneous adsorption, with their magnitudes reflecting adsorption strength. Stronger

interactions with the (11–1) crystal face indicate that HPMC and HPC exhibit clear face selectivity, which aligns with experimental results. HPMC and HPC markedly suppress the crystal growth rate perpendicular to the (11–1) crystal face while comparatively promoting crystal growth along other crystallographic directions. In contrast, PAM shows comparable interaction strengths on the (11–1) and (011) crystal faces, resulting in similar inhibition effects. These simulation results are also in good agreement with the experimental crystal growth rates.

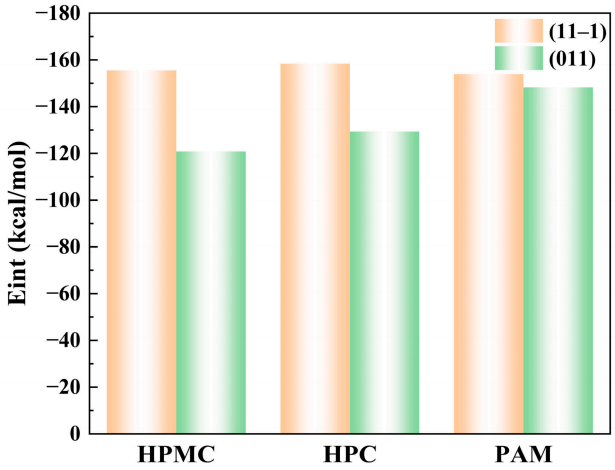


Figure 12. Comparative analysis of interaction energies between crystal faces and polymeric additives.

3.4.2. Concentration Distribution of Molecules near Crystal Faces

In practical crystallization systems, crystal growth occurs within the solid–liquid interfacial region; consequently, the spatial distribution of molecules near crystal faces plays a critical role in the crystallization process.

As shown in Figure 13, in the pure water system, most GAA molecules migrate toward and adsorb onto the (11–1) crystal face after equilibration. In the presence of PAM, only a fraction of solute molecules resides near the crystal surface, while the majority remain in the bulk solution. In contrast, in HPMC and HPC systems, nearly all solute molecules are confined to the bulk phase, with negligible contact with the crystal surface.

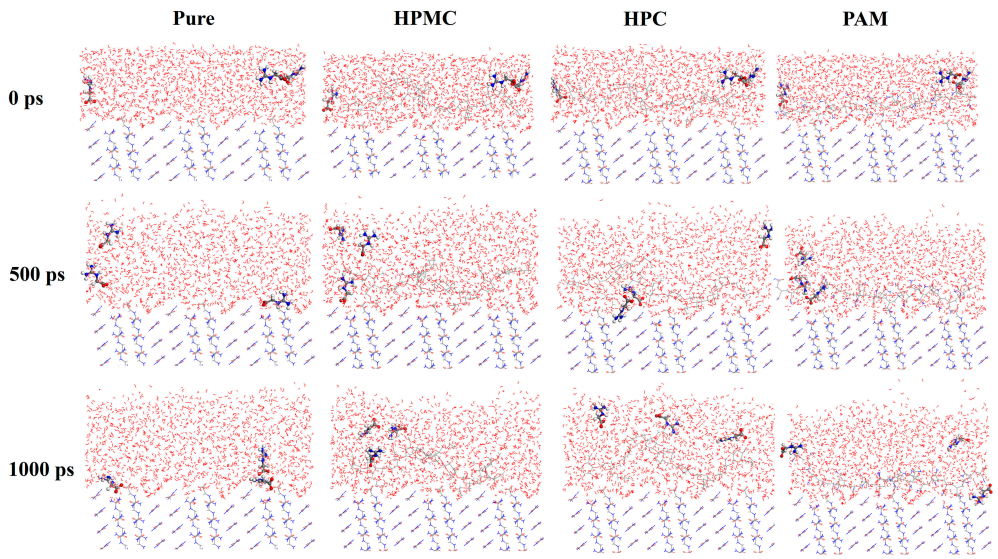


Figure 13. Diffusion dynamics of GAA molecules (represented by ball-and-stick models) on the (11–1) crystal face under various additive conditions (The lower layer is the crystal face of GAA, while the upper layer is the solution layer. The red part represents water.).

Figure S12 illustrates the molecular distribution in the vicinity of the (011) crystal face. In systems containing HPMC or HPC, a portion of GAA molecules was observed to adsorb near the crystal face following the simulation. In contrast, solute molecules were scarcely detected on the crystal surface in the PAM system.

Furthermore, an analysis of the concentration distribution of solute or additive molecules near the crystal faces was conducted to provide a more intuitive demonstration of interfacial behavior.

Figure 14 illustrates that solute molecules are predominantly distributed within a range of approximately 37–65 Å from the bottom of the crystal layer, a thickness that closely aligns with that of the solution layer. Moreover, a non-uniform distribution of solute concentration near the crystal faces is observed. In proximity to the (11–1) crystal face, the order of solute concentration from high to low follows: Pure > PAM > HPC > HPMC. Conversely, near the (011) crystal face, the concentration trend is HPMC > HPC > Pure > PAM. These trends are consistent with the distribution tendencies of GAA molecules on the crystal surfaces as presented in Figures 13 and S12.

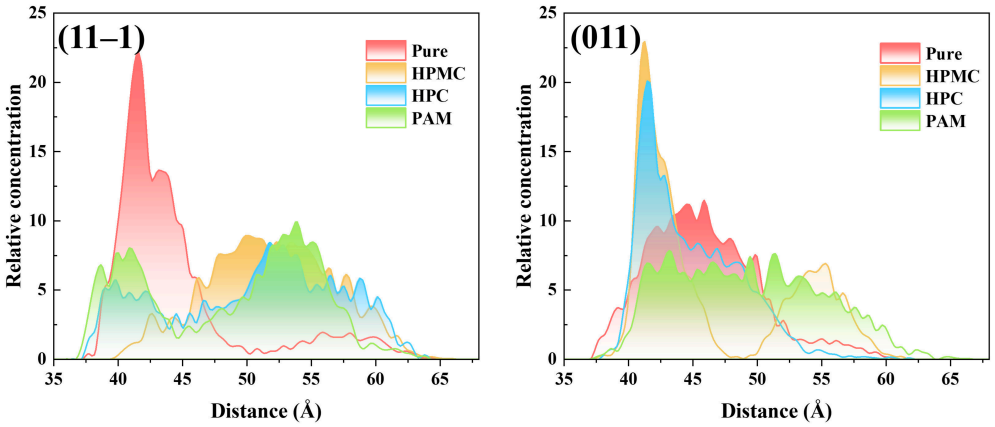


Figure 14. Concentration distribution of GAA along the normal direction to the crystal face.

Notably, as shown in Figures 14 and 15, in the PAM system on the (11–1) crystal face and the HPMC system on the (011) face, solute concentration exhibits distinct troughs, while the concentration of additive molecules is significantly elevated in the corresponding regions. The phenomenon that higher solute concentrations typically correlate with lower additive concentrations—and vice versa—is widely observed across diverse systems. These findings indicate that the adsorption of additives near crystal surfaces can alter the spatial distribution of solute molecules in the solution. This, in turn, affects solute transport and incorporation into crystal surfaces, thereby modulating crystal growth behavior.

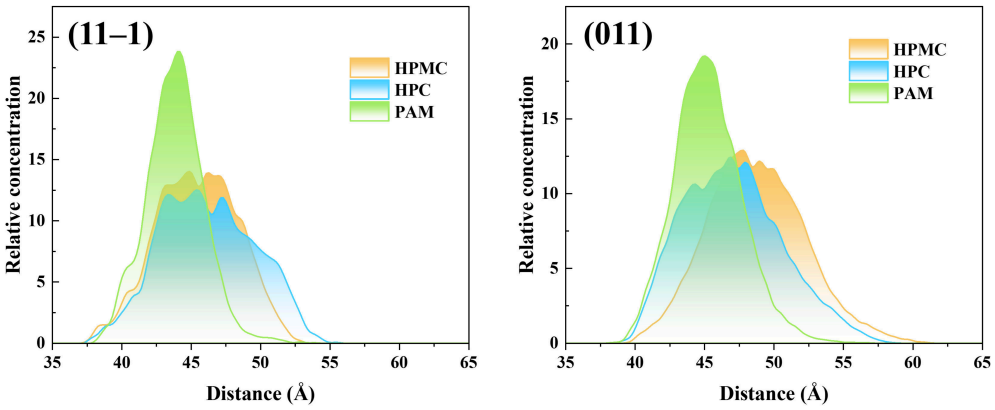


Figure 15. Concentration distribution of additives along the normal direction to the crystal face.

3.4.3. Effect of Additives on Solute Diffusion

The Mean Squared Displacement (MSD) characterizes the migration capacity of solute molecules in solution, thereby providing kinetic insights into the mass transfer behavior from the bulk solution to the crystal interface.

As shown in Figure 16, on the (11–1) crystal face, the MSD of GAA molecules in the presence of different additives follows the order: HPMC > HPC > PAM > Pure. Interestingly, this trend is the complete opposite of the experimentally determined absolute growth rates on the (11–1) crystal face. A similar trend is observed on the (011) crystal face.

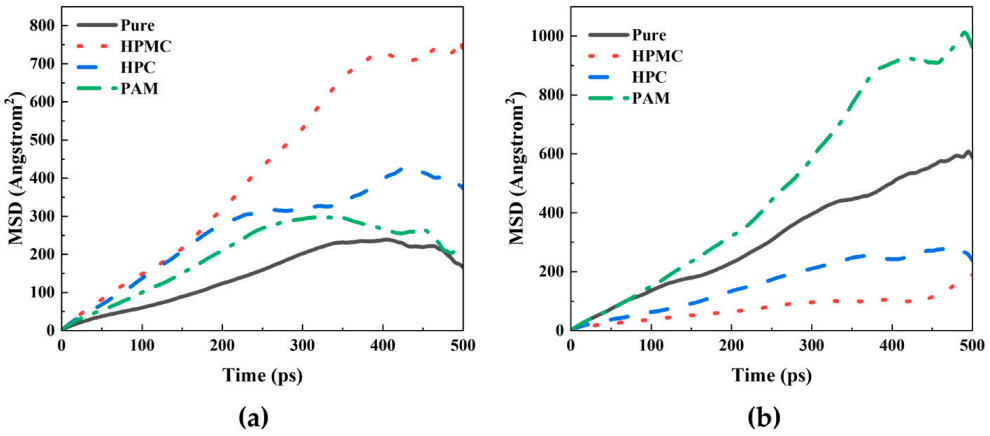


Figure 16. MSD of GAA molecules under various additive conditions: (**a**) (11–1) crystal face, (**b**) (011) crystal face.

Combining the aforementioned results on molecular distribution near the crystal faces, we find that when additives are adsorbed onto the crystal faces, they attenuate the enrichment or adsorption of solute molecules adjacent to the crystal surface to varying degrees. As a result, solute molecules tend to exhibit a greater propensity to remain as free entities in the bulk solution rather than adsorbing onto the additives. This enhances the overall diffusivity of the solute molecules; however, their probability of incorporation into the crystal face is diminished, ultimately suppressing crystal growth.

3.4.4. Additive-Mediated Morphology Control Mechanism

Based on the analysis of interaction energy, interfacial concentration distribution, and mean squared displacement, a molecular mechanism has been developed to elucidate how polymeric additives regulate GAA crystal growth and influence crystal morphology, as illustrated in Figure 17.

HPMC and HPC exhibit markedly different adsorption behaviors across crystal faces, both demonstrating a clear preference for the (11–1) crystal face of GAA. This selective adsorption alters the local solid–liquid interfacial environment, leading to the formation of an additive-enriched layer that reorganizes the molecular distribution near the crystal surface. Owing to their strong affinity for the (11–1) crystal face, HPMC and HPC suppress solute accumulation and interfacial transport in its vicinity, thereby reducing its growth rate. In turn, solute molecules are more likely to migrate toward and accumulate on the (011) and (001) crystal faces, enhancing their growth rates. At the macroscopic level, this manifests as a significant reduction or even disappearance of the (011) crystal face, along with enhanced growth along the normal direction of the (001) crystal face. Ultimately, the morphology of GAA crystals transforms from hexagonal plate-like crystals in pure water to quadrangular block-like crystals.

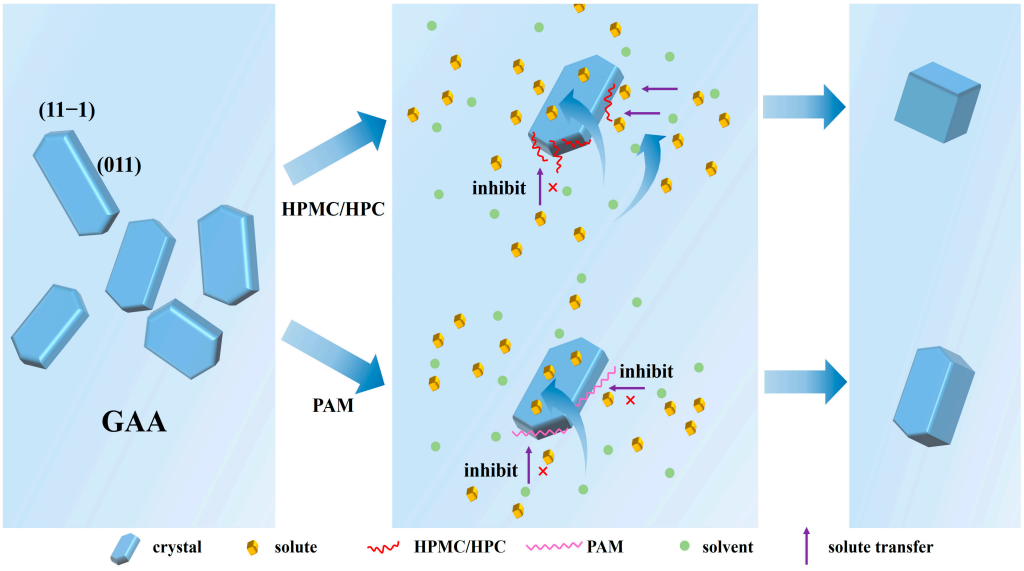


Figure 17. Mechanism of additive-induced morphological control of GAA.

As for the PAM system, although PAM molecules exhibit relatively strong adsorption on both the (11–1) and (011) crystal faces and partially hinder the accumulation of solute molecules near the crystal surfaces, their comparable adsorption strengths on these two faces do not significantly alter the relative growth rates of the faces. As a result, the crystal retains the hexagonal morphology defined by the (001) crystal face. However, the enhanced accumulation of solute molecules near the (001) crystal face accelerates growth along its normal direction, leading to a morphological evolution from hexagonal plate-like crystals in pure water to thicker hexagonal plate-like crystals.

3.5. Characterization of GAA Powder Properties

3.5.1. Particle Size Distribution

To assess the practical application potential of HPMC, HPC, and PAM, the effect of different polymeric additives on the particle size distribution of GAA products was first examined, with the results presented in Figure 18. To enhance the controllability of the crystallization process and approximate actual production conditions, 0.5 wt% of seed crystals was introduced during the experiment.

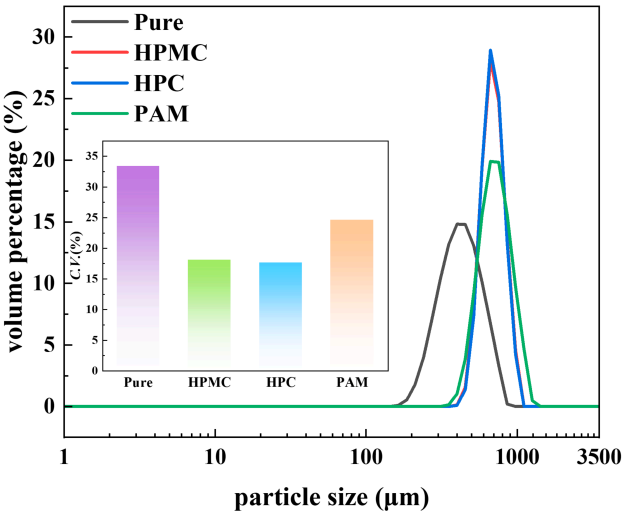


Figure 18. Particle size distribution of GAA products under various additive conditions.

The results demonstrate that the introduction of additives leads to an overall increase in crystal particle size compared with the pure water system. The majority of crystal particles obtained with additives fall within the range of 500–1000 μm, whereas those produced in the pure water system are predominantly concentrated in the 200–800 μm range. These findings are consistent with the observations presented in Figure 5, confirming that the introduction of additives results in a significant enlargement of crystal particle dimensions.

The uniformity of the products was further evaluated using the coefficient of variation (*C.V.*). Figure 18 shows that the product from the pure water system had an intermediate *C.V.*, and the PAM system yielded a *C.V.* of approximately 25%. The bulk crystals formed in the presence of HPMC and HPC showed a *C.V.* within the range of 15–20%, indicating a more concentrated particle size distribution compared with the pure water system.

From the perspective of crystallization kinetics, the three selected additives alter the crystal growth behavior by preferentially inhibiting the growth of specific crystal faces while relatively promoting the development of others. This face-selective modulation thereby leads to increased crystal size. However, secondary nucleation during crystallization generates new crystal particles, significantly influencing the final particle size distribution. To further elucidate the underlying causes of crystal enlargement under additive influence, the secondary nucleation induction times across different systems were experimentally determined. As depicted in Figure 19, after seeding, the particle number remains nearly constant at the initial stage, during which crystal growth proceeds via consumption of supersaturation. The secondary nucleation induction times follow the trend: Pure < PAM ≤ HPC < HPMC. Compared with the pure water system, all additives delay the secondary nucleation of GAA to some extent, with HPMC exhibiting more pronounced delay effects. This allows GAA crystals to have sufficient time to grow by consuming supersaturation. Qualitative results of the secondary nucleation process of GAA crystals in solution indicate that the three selected polymer additives increase the crystal size of GAA to a certain extent by delaying the onset of secondary nucleation.

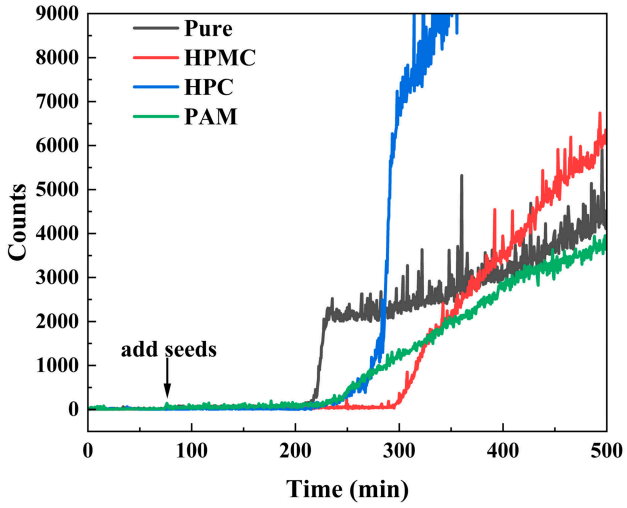


Figure 19. The secondary nucleation process of systems in the presence and absence of additives.

The combination of crystal growth rate and secondary nucleation behavior indicates that the addition of polymeric additives significantly alters the crystallization kinetics of GAA. On the one hand, selective adsorption of additives on specific crystal faces modulates growth rates, which promotes a transition from plate-like to block-like and elongation along the c-axis, thereby facilitating crystal enlargement. On the other hand, additives retard secondary nucleation, diverting supersaturation from nucleation to crystal growth.

Consequently, larger crystal sizes and a narrower particle size distribution are obtained in the presence of additives.

3.5.2. Flowing Performance and Anti-Caking Performance

As presented in Table 1, the GAA products obtained in the presence of additives exhibit a Carr Compressibility Index (*CI*) below 15% and a Hausner Ratio (*HR*) below 1.35. Furthermore, the angle of repose of the products is reduced compared with that of the GAA product obtained in the pure water system, indicating favorable flow characteristics. Density measurements reveal an increase in both the bulk density and the tapped density of the regulated products, with a small difference between the two densities. This suggests that the compaction of the powder under external force is limited, resulting in a relatively stable particle packing structure. These properties not only contribute to enhanced packaging efficiency but also reduce volume-related costs during storage and transportation.

Table 1. Powder properties of GAA products.

	Angle of Repose (○)	CI (%)	HR	Bulk Density (g/cm^3)	Tapped Density (g/cm^3)
HPMC	29.93	3.037	1.031	0.830	0.856
HPC	29.71	2.881	1.030	0.809	0.833
PAM	32.54	2.645	1.027	0.773	0.794
Pure	32.95	5.375	1.057	0.757	0.800
raw material	37.12	26.901	1.368	0.375	0.513

The test results for the caking ratio of GAA products (Figure 20) indicate that the product with a modified block-like crystal morphology exhibits superior anti-caking performance, with a caking ratio of approximately 0.42%. This improvement is primarily attributed to the reduced interparticle contact area and weakened adhesion forces among the block-like crystals, which diminish the caking tendency. A lower caking ratio reflects the enhanced dispersibility of the product, facilitating more uniform distribution of GAA during feed premixing. This contributes to improved homogeneity of feed formulations and ensures consistent intake of active ingredients by animals.

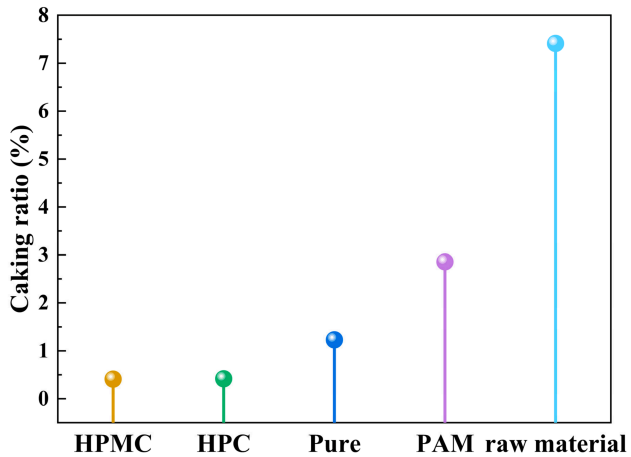


Figure 20. Caking ratio of GAA products obtained under different additives.

In comparison, the products prepared with the pure water system and the PAM system exhibit a slightly higher caking ratio, which yet remains within an acceptable range and has negligible impact on practical applications. During the feed production process, mechanical mixing and conveying operations can effectively disrupt weak agglomerates, thereby limiting the influence of such caking on the product's actual application performance.

4. Conclusions

In this work, a combined experimental and molecular dynamics simulation approach was employed to systematically elucidate the regulatory mechanisms of three polymeric additives on the crystal growth of GAA. The results indicate that, under experimental conditions, all additives exert negligible influence on solubility, suggesting that the observed morphological variations are not governed by changes in solution supersaturation. In the presence of HPMC and HPC, the crystal morphology transforms from hexagonal plate-like shapes in pure water to quadrangular block-like shapes. In contrast, PAM has a limited impact on crystal morphology but promotes growth along the c-axis of GAA crystals, resulting in increased crystal thickness.

In situ single-crystal growth experiments reveal distinct modulation effects of different additives on crystal face growth. HPMC and HPC suppress the absolute growth rate of the (11–1) crystal face while enhancing that of the (011) crystal face, thereby altering the relative growth rates. By comparison, PAM inhibits the growth of both (11–1) and (011) crystal faces, with minimal influence on their relative growth relationship. Growth kinetic analysis demonstrates that crystal growth is predominantly controlled by the surface integration step, with the B&S model providing the best fit to the experimental data.

Molecular dynamics simulations reveal that both HPMC and HPC exhibit strong affinity toward the (11–1) crystal face, thereby suppressing solute accumulation and interfacial transport in its vicinity, which leads to a reduction in its absolute growth rate. Consequently, solute molecules preferentially migrate toward and accumulate on the (011) and (001) crystal faces, resulting in an enhancement of their growth rates. As a result of this anisotropic growth behavior, the (011) crystal face gradually diminishes or even disappears, while the relative area fraction of the (11–1) crystal face increases significantly in the final crystal morphology. In contrast, although PAM shows appreciable adsorption on both the (11–1) and (011) crystal faces, its lack of crystallographic selectivity renders its influence on the relative solute transport toward these faces negligible. As such, PAM exerts minimal impact on the morphology of GAA crystals.

Additionally, the presence of additives delays secondary nucleation and regulates crystal growth, directing supersaturation toward the growth of existing crystals. As a result, larger crystal sizes with a narrower particle size distribution are achieved. Powder property measurements further confirm that block-like crystals exhibit reduced caking tendency, improved flowability, and higher bulk density, which are advantageous for downstream processing, separation and filtration, storage, and feed applications.

This study provides a comprehensive understanding of the roles of polymeric additives in crystal growth and establishes a mechanistic framework capable of explaining their distinct effects. The insights gained herein offer valuable guidance for the computational screening and rational design of additives, thereby facilitating their practical application in crystallization processes.

Supplementary Materials: The following supporting information can be downloaded at: https://www.mdpi.com/article/10.3390/separations13060159/s1, Figure S1. The scheme of the establishment of the vacuum–additive–crystal model; Figure S2. Variation in temperature and total energy with simulation time; Figure S3. DSC curve of GAA; Figure S4. Solubility curves fitted by the NRTL equation; Figure S5. The plot of the relative distance as a function of time at $\sigma = 0.35$: (a) (11–1) crystal face; (b) (011) crystal face.; Figure S6. Fitted curves of the BCF model for GAA acid crystal growth data: (a) (11–1) crystal face, (b) (011) crystal face; Figure S7. Fitted curves of the RIG model for GAA crystal growth data: (a) (11–1) crystal face, (b) (011) crystal face; Figure S8. Residual analysis of the BCF model; Figure S9. Residual analysis of the B&S model; Figure S10. Residual analysis of the RIG model; Figure S11. Residual analysis of the empirical equation.; Figure S12. Diffusion dynamics of GAA molecules (represented by ball-and-stick models) on the (011) crystal face under various

additive conditions during the simulation; Table S1. Detailed information on the chemical materials; Table S2. The solubility of GAA at different additives; Table S3. Fitting parameters of the modified Apelblat equation; Table S4. Fitting parameters of the NRTL equation; Table S5. Fitting parameters for the BCF model; Table S6. Fitting parameters for the B&S model; Table S7. Fitting parameters for the RIG model; Table S8. Fitting parameters for the empirical equation.

Author Contributions: Conceptualization, X.C.; methodology, X.C. and T.W.; software, X.C. and N.W.; validation, X.C. and L.Z. and H.H.; formal analysis, X.C., T.W. and N.W.; investigation, X.C.; resources, L.Z., H.H. and J.W.; writing—original draft preparation, X.C.; writing—review and editing, L.Z. and T.W.; visualization, X.C., Y.L. and Q.W.; data curation, X.C., Y.L. and Q.W.; supervision, L.Z., H.H. and J.W. All authors have read and agreed to the published version of the manuscript.

Funding: This research was funded by the National Key Research and Development Program of China (No: 2024YFC3908505-02).

Data Availability Statement: The original contributions presented in this study are included in the article. Further inquiries can be directed to the corresponding authors.

Conflicts of Interest: The authors declare no conflicts of interest.

Abbreviations

The following abbreviations are used in this manuscript:

GAA	Guanidinoacetic Acid
HPMC	Hydroxypropyl Methyl Cellulose
HPC	Hydroxypropyl Cellulose
PAM	polyacrylamide
ARD	average relative deviation
RMSD	root-mean-square deviation
SEM	scanning electron microscopy
PXRD	Powder X-ray diffraction
FTIR	Fourier transform infrared
NMR	nuclear magnetic resonance
C.V.	coefficient of variation
PSD	particle size distribution
CI	Carr Compressibility Index
HR	Hausner Ratio
MSD	Mean Squared Displacement

References

1. Cui, P.; Liu, Y.; Jia, L.; Zhou, L.; Yin, Q. How Do Morphological Changes of Caffeine Hydrate Influence Caking. *J. Food Eng.* **2023**, *344*, 111393. [CrossRef]
2. Huo, X.; Guo, L.; Liu, R.; Tao, C.; Xi, B. Role of Additives: Modified Hemihydrate Phosphogypsum Morphology and Enhanced Filtration Performance of Wet-Process Phosphoric Acid. *ACS Omega* **2023**, *8*, 47295–47303. [CrossRef]
3. Jin, J.; Yurkow, E.J.; Adler, D.; Lee, T.-C. Improved Freeze Drying Efficiency by Ice Nucleation Proteins with Ice Morphology Modification. *Food Res. Int.* **2018**, *106*, 90–97. [CrossRef]
4. Turner, T.D.; Gajjar, P.; Fragkopoulos, I.S.; Carr, J.; Nguyen, T.T.H.; Hooper, D.; Clarke, F.; Dawson, N.; Withers, P.J.; Roberts, K.J. Measuring the Particle Packing of L-Glutamic Acid Crystals through X-Ray Computed Tomography for Understanding Powder Flow and Consolidation Behavior. *Cryst. Growth Des.* **2020**, *20*, 4252–4263. [CrossRef]
5. Qi, J.; Meng, W.; An, K.; Hui, X.; Liu, L.; Ma, Y.; Li, N. Regulating the Morphology of Two-Dimensional Perovskite Single-Crystals via High-Throughput Experimentations. *Nat. Commun.* **2025**, *16*, 11518. [CrossRef]
6. Langer, J.; Jimenez De Aberasturi, D.; Aizpurua, J.; Alvarez-Puebla, R.A.; Auguié, B.; Baumberg, J.J.; Bazan, G.C.; Bell, S.E.J.; Boisen, A.; Brolo, A.G.; et al. Present and Future of Surface-Enhanced Raman Scattering. *ACS Nano* **2020**, *14*, 28–117. [CrossRef] [PubMed]
7. Willets, K.A.; Van Duyne, R.P. Localized Surface Plasmon Resonance Spectroscopy and Sensing. *Annu. Rev. Phys. Chem.* **2007**, *58*, 267–297. [CrossRef]

8. Jiang, Y.; Zai, H.; Zheng, X.; Zhang, Y.; Faheem, M.B.; Dai, S.; Lv, Z.; Ma, Y.; Li, L.; Tao, Y.; et al. Fused-Ring Electron Acceptors as a Versatile Additive Platform for Efficient Perovskite Photovoltaics. *J. Am. Chem. Soc.* **2026**, *148*, 1041–1050. [CrossRef]
9. Zhao, J.; Wang, N.; Wang, J.; Ji, X.; Li, J.; Li, A.; Huang, X.; Wang, T.; Zhou, L.; Hao, H. Recent Progress on Strategies for the Enhancement of Crystal Growth Process. *CrystEngComm* **2023**, *25*, 2688–2700. [CrossRef]
10. Kim, Y.; Freeman, C.L.; Gong, X.; Levenstein, M.A.; Wang, Y.; Kulak, A.; Anduix-Canto, C.; Lee, P.A.; Li, S.; Chen, L.; et al. The Effect of Additives on the Early Stages of Growth of Calcite Single Crystals. *Angew. Chem. Int. Ed.* **2017**, *56*, 11885–11890. [CrossRef]
11. Pan, Z.; Cao, X.; Ke, W.; Wang, J.; Wang, Y.; Du, S.; Xue, F. Effect of Additives on the Morphology of γ-Aminobutyric Acid Crystals. *ACS Omega* **2024**, *9*, 29928–29938. [CrossRef]
12. Lechuga-Ballesteros, D.; Rodriguez-Hornedo, N. Growth and Morphology of L-Alanine Crystals: Influence of Additive Adsorption. *Pharm. Res.* **1993**, *10*, 1008–1014. [CrossRef] [PubMed]
13. Singh, N.; Yeri, R.; Chakraborty, J. Effect of Ionic Surfactants and Alcohols on the Morphology of $CuSO_4 \cdot 5H_2O$ Crystals: Combined Use of Factors and Significance of Threshold Surfactant Concentration. *Ind. Eng. Chem. Res.* **2013**, *52*, 15041–15048. [CrossRef]
14. Sun, R.; Gao, Y.; Jiao, X.; Jiao, C.; Liu, L.; Peng, J.; Shi, Y.; Hu, X.; Dong, J.; Shi, W.; et al. Molecular Engineering of Functionalized Amino-Acid Additives for Synergistic Stabilization of Zinc Metal Anode. *Small* **2026**, *22*, e13740. [CrossRef] [PubMed]
15. Anuar, N.; Wan Daud, W.R.; Roberts, K.J.; Kamarudin, S.K.; Tasirin, S.M. Morphology and Associated Surface Chemistry of L-Isoleucine Crystals Modeled under the Influence of L-Leucine Additive Molecules. *Cryst. Growth Des.* **2012**, *12*, 2195–2203. [CrossRef]
16. Zhao, K.; Liu, P.; Li, K.; Zhang, Y.; Cao, J.; Cheng, J.; Yang, C. Effect of Polyethylene Glycol Additives on the Polymorph and Crystal Habit of Carbamazepine. *J. Cryst. Growth* **2022**, *588*, 126644. [CrossRef]
17. Han, Y.; Yang, P.; Liu, Y.; Wu, S.; Gong, J. Effects of Polymers on the Regulation of P-Aminobenzoic Acid Crystal Habit. *J. Mol. Liq.* **2023**, *380*, 121748. [CrossRef]
18. Nicolau, S.T.; Matzger, A.J. Controlling Energetic Crystal Morphology Using Tailored Polymeric Additives. *Cryst. Growth Des.* **2025**, *25*, 1667–1674. [CrossRef]
19. Bellucci, M.A.; Marx, A.; Wang, B.; Fang, L.; Zhou, Y.; Greenwell, C.; Li, Z.; Becker, A.; Sun, G.; Brandenburg, J.G.; et al. Effect of Polymer Additives on the Crystal Habit of Metformin HCl. *Small Methods* **2023**, *7*, 2201692. [CrossRef]
20. Hatcher, L.E.; Li, W.; Payne, P.; Benyahia, B.; Rielly, C.D.; Wilson, C.C. Tuning Morphology in Active Pharmaceutical Ingredients: Controlling the Crystal Habit of Lovastatin through Solvent Choice and Non-Size-Matched Polymer Additives. *Cryst. Growth Des.* **2020**, *20*, 5854–5862. [CrossRef]
21. Tan, M.; Huang, X.; Song, W.; Wang, T.; Wang, N.; Bai, X.; Wang, Q.; Yu, H.; Zhou, L.; Hao, H. Uncovering the Coupling Mechanism of Enhanced Growth of Acephate by Additives: Experiments and Molecular Dynamics Simulations. *Cryst. Growth Des.* **2023**, *23*, 8426–8435. [CrossRef]
22. Furukawa, Y.; Nagashima, K.; Nakatsubo, S.; Yoshizaki, I.; Tamaru, H.; Shimaoka, T.; Sone, T.; Yokoyama, E.; Zepeda, S.; Terasawa, T.; et al. Oscillations and Accelerations of Ice Crystal Growth Rates in Microgravity in Presence of Antifreeze Glycoprotein Impurity in Supercooled Water. *Sci. Rep.* **2017**, *7*, 43157. [CrossRef]
23. Zhang, B.; Liu, N.; Kang, K.; Zhang, R.; Hao, M.; Song, P.; Wang, Q.; Xie, Y.; Li, C. Dietary Guanidineacetic Acid Supplementation Ameliorated Meat Quality and Regulated Muscle Metabolism of Broilers Subjected to Pre-Slaughter Transport Stress by Metabolomics Analysis. *Poult. Sci.* **2022**, *101*, 101739. [CrossRef] [PubMed]
24. Khajali, F.; Lemme, A.; Rademacher-Heilshorn, M. Guanidinoacetic Acid as a Feed Supplement for Poultry. *World's Poult. Sci. J.* **2020**, *76*, 270–291. [CrossRef]
25. Martinez, E.J.; Wong, D.H.; Patel, A.J.; Vaz, R.J.; Busby, R.W.; Zahler, R.; Schefer, D.; Zhao, H.; Xu, X.; Liu, Z.; et al. Carboxylic Acid Bioisosteres of Creatine as Novel and Selective Substrate Competitive Inhibitors of the Creatine Transporter SLC6A8. *J. Med. Chem.* **2026**, *69*, 3915–3931. [CrossRef]
26. Bai, Z.; Liu, Q.; Zhang, H.; Liu, J.; Yu, J.; Wang, J. A Novel 3D Reticular Anti-Fouling Bio-Adsorbent for Uranium Extraction from Seawater: Polyethylenimine and Guanidyl Functionalized Hemp Fibers. *Chem. Eng. J.* **2020**, *382*, 122555. [CrossRef]
27. Ma, J.; Xu, H.; Zhang, M.; Wang, J.; Lin, T.; Tao, H. Guanidineacetic Acid Dual-Regulated Interfacial Polymerization towards Highly Permeable and Ultraselective Nanofiltration Membranes. *J. Membr. Sci.* **2026**, *738*, 124889. [CrossRef]
28. Vraneš, M.; Ostojić, S.; Tot, A.; Papović, S.; Gadžurić, S. Experimental and Computational Study of Guanidinoacetic Acid Self-Aggregation in Aqueous Solution. *Food Chem.* **2017**, *237*, 53–57. [CrossRef]
29. Srivastava, N.; Bansal, A.; Aggarwal, K.; Nagpal, K. Development and Validation of UV Spectrophotometric Method for the Quantitative Estimation of Quercetin in Bulk Followed by Its Solubility Studies. *J. Appl. Spectrosc.* **2024**, *91*, 700–708. [CrossRef]
30. Cheng, Y.; Wang, X.; Liu, W.; Wang, D.; Chen, L. Experimental Measurement and Correlation of the Solubility of Aloe-Emodin in Seven Pure Solvents. *J. Chem. Thermodyn.* **2016**, *98*, 51–55. [CrossRef]

31. Li, W.; Cui, Z.; Jiang, Y.; Aisikaer, A.; Wu, Q.; Zhang, F.; Wang, W.; Bo, Y.; Yang, H. Dietary Guanidine Acetic Acid Improves Ruminal Antioxidant Capacity and Alters Rumen Fermentation and Microflora in Rapid-Growing Lambs. *Antioxidants* **2023**, *12*, 772. [CrossRef] [PubMed]
32. Renon, H.; Prausnitz, J.M. Local Compositions in Thermodynamic Excess Functions for Liquid Mixtures. *AIChE J.* **1968**, *14*, 135–144. [CrossRef]
33. Mukhopadhyay, I.; Mohandas, V.P.; Desale, G.R.; Chaudhary, A.; Ghosh, P.K. Crystallization of Spherical Common Salt in the Submillimeter Size Range without Habit Modifier. *Ind. Eng. Chem. Res.* **2010**, *49*, 12197–12203. [CrossRef]
34. Kedia, K.; Wairkar, S. Improved Micromeritics, Packing Properties and Compressibility of High Dose Drug, Cycloserine, by Spherical Crystallization. *Powder Technol.* **2019**, *344*, 665–672. [CrossRef]
35. Chen, M.; Wu, S.; Tang, W.; Gong, J. Caking and Adhesion Free Energy of Maltitol: Studying of Mechanism in Adhesion Process. *Powder Technol.* **2015**, *272*, 235–240. [CrossRef]
36. Cleaver, J.A.S.; Karatzas, G.; Louis, S.; Hayati, I. Moisture-Induced Caking of Boric Acid Powder. *Powder Technol.* **2004**, *146*, 93–101. [CrossRef]
37. Burton, W.K.; Cabrera, N.; Frank, F.C. The Growth of Crystals and the Equilibrium Structure of Their Surfaces. *Philos. Trans. R. Soc. Lond. Ser. A Math. Phys. Sci.* **1951**, *243*, 299–358. [CrossRef]
38. Lynch, A.; Jia, L.; Svärd, M.; Rasmuson, Å.C. Crystal Growth of Salicylamide in Organic Solvents. *Cryst. Growth Des.* **2018**, *18*, 7305–7315. [CrossRef]
39. Nguyen, T.T.H.; Hammond, R.B.; Roberts, K.J.; Marziano, I.; Nichols, G. Precision Measurement of the Growth Rate and Mechanism of Ibuprofen {001} and {011} as a Function of Crystallization Environment. *CrystEngComm* **2014**, *16*, 4568–4586. [CrossRef]
40. Gao, Q.; Ai, J.; Tang, S.; Li, M.; Chen, Y.; Huang, J.; Tong, H.; Xu, L.; Xu, L.; Tanaka, H.; et al. Fast Crystal Growth at Ultra-Low Temperatures. *Nat. Mater.* **2021**, *20*, 1431–1439. [CrossRef]
41. Nambiar, H.N.; Zamborini, F.P. Size-Dependent Electrochemical Metal Growth Kinetics. *J. Phys. Chem. C* **2023**, *127*, 4087–4095. [CrossRef]
42. Stranski, I.N. Zur Theorie Des Kristallwachstums. *Z. Für Phys. Chem.* **1928**, *136U*, 259–278. [CrossRef]
43. Cahn, J.W. Theory of Crystal Growth and Interface Motion in Crystalline Materials. *Acta Metall.* **1960**, *8*, 554–562. [CrossRef]
44. Roberts, K.J.; Elwell, D. Correlation between Growth Hillocks and Dislocations on the {110} Faces of Flux Grown Yttrium Aluminium Garnet. *J. Cryst. Growth* **1983**, *62*, 449–457. [CrossRef]
45. Friedel, M.G. Études Sur La Loi de Bravais. *Bull. De Minéralogie* **1907**, *30*, 326–455. [CrossRef]
46. Donnay, J.D.H.; Harker, D. A New Law of Crystal Morphology Extending the Law of Bravais. *Am. Mineral.* **1937**, *22*, 446–467.
47. Yan, N.; Fu, Q.; Zhang, J.; Shen, Q. Two-Dimensional Nucleation Growth of Stepped ZrC Skeleton with Controllable Morphology. *Ceram. Int.* **2021**, *47*, 19090–19097. [CrossRef]
48. Chen, P.; Shen, W.; Chen, Z.; Li, C.; Han, S.; Wu, Y.; Hang, T.; Li, M. Surface Atom Migration-Involved Two-Dimensional Nucleation and Growth of Nanotwinned Copper in DC Electrodeposition. *Acta Mater.* **2024**, *262*, 119468. [CrossRef]
49. Parker, R.L. Modeling Crystal Growth Rates from Solution. *J. Cryst. Growth* **1974**, *22*, 335–338. [CrossRef]

Disclaimer/Publisher's Note: The statements, opinions and data contained in all publications are solely those of the individual author(s) and contributor(s) and not of MDPI and/or the editor(s). MDPI and/or the editor(s) disclaim responsibility for any injury to people or property resulting from any ideas, methods, instructions or products referred to in the content.